

## Fully dynamic computer simulation of self-interstitial diffusion in tungsten\*

M. W. Guinan, R. N. Stuart, and R. J. Borg

*Lawrence Livermore Laboratory, University of California, Livermore, California 94550*

(Received 7 June 1976)

A fully dynamic model of interstitial diffusion in W yields an energy of activation in good agreement with the static relaxation method. However, random-walk statistics are inapplicable except for large diffusion distances; correlation effects are strong and clearly temperature dependent. The latter observations are reconciled with the spatial configuration of the static potential to give a self-consistent explanation.

### I. INTRODUCTION

Because of the technological importance of radiation-induced damage and because self-interstitial atoms are the immediate consequence of a damage event, they have received considerable attention over the years. The temperature-independent static relaxation method has most often been used in computer simulations, and in only one case, to the best of our knowledge, has the motion of an interstitial been followed to the extent that a diffusion coefficient could be measured. We have employed a fully dynamic model to examine in quantitative detail interstitial diffusion in tungsten metal and to obtain the activation energy by applying the Arrhenius relationship to the measured values. We then have computed the activation energy by conventional static methods, using the same potential. A comparison of the two results provides convincing support for the validity of the static model, but significant and unexpected details of the jump process are revealed by the dynamic calculation.

Tsai, Bullough, and Perrin<sup>1</sup> (TBP) created a dynamic model to investigate interstitial and vacancy diffusion in bcc  $\alpha$  Fe, and they found good agreement with the static-model values of the activation energy for interstitial diffusion. In this investigation, a major improvement in statistics and a clearer delineation of the kinematics have been achieved. Tsai and Bullough found it necessary to perform all of their computations above the  $\alpha$ - $\gamma$  transition temperature to obtain a reasonable number of jumps in the prescribed counting period and, in fact, most are above the true melting point of Fe. Our computations span a realistic range in reduced temperature, in which  $T/T_m < 1$  always obtains, and they reveal new complexities in the many-body detailed mechanism of the diffusive displacement.

The method by which one defines and counts jumps is critical for obtaining correct values of  $D_0$  and  $\Delta H_m^+$ , and the previous counting procedures are apparently incorrect. This accounts for the

spuriously high value of the jump rate at the lowest temperature, and will be discussed in detail in a later section of this report. Suffice it to say here that jumps defined in terms of residence times give incorrect results.

Our code is completely general, and thus it can be used to calculate any relevant lattice dynamic property. It is easily modified to accommodate alternative potentials, and with slightly greater effort, the program can be adapted to handle the fcc structure. The selection of tungsten was based upon our reliance on the pair potential<sup>2</sup> supplied to us by Wilson, and our desire to study bcc crystals, which are more important technologically than fcc materials.

### II. MODEL

Our decision to use a potential function appropriate for tungsten metal was based upon the fact that it best reproduces the experimentally measured phonon dispersion data and also satisfies our stated desire to study bcc materials. As our major objective was to compare the dynamic with the static model, attaining a most accurate representation of the vibrational spectrum appeared of utmost importance. The potentials are described in detail elsewhere<sup>2</sup>; however, to summarize briefly, the potentials that extend pairwise to include nearest and next nearest neighboring atoms are determined at near equilibrium separations by fitting to the elastic constants. The structure is constrained by an externally imposed hydrostatic pressure of 0.2 Mb selected to match the elastic constants and atomic volume at 0 K.

A centered first-order finite-difference scheme is used to solve the equations of motion in successive time steps. The time step  $\Delta t$  is taken equal to  $\frac{1}{15}$  the value of the reciprocal of the maximum lattice vibrational frequency  $\nu_{\max}$ . This time interval is sufficiently large to facilitate completion of the problem in a reasonable period of time, and yet small enough to give accurate results. The

reliability has been tested by reducing the time step by a factor of 10, i.e.,  $t = \frac{1}{150} \nu_{\max}^{-1}$ , and by verifying in sample calculations that one obtains the same values for the interstitial jump rate as with the longer time step.

As shown in Fig. 1, the model employs a block of  $2 \times 9^3$  atoms, corresponding to  $10 \times 10 \times 10$  cubic cells serving as the defect-containing matrix; periodic boundary conditions effectively provide an infinite extension of the structure. Survey calculations of the static potential were made on a block  $7 \times 7 \times 7$ . Both cells shown in Fig. 1 surround a single unit containing a split interstitial and show the relative scale of the entire calculation. The shape of the fundamental unit was varied in test calculations to ensure that non-physical periodic vibrational modes were absent. An extremely distorted unit, having dimensions  $10 \times 10 \times 25$  cells, still gave the same values for the jump frequency.

The system is initialized by giving each atom random velocity components and by allowing sufficient time for the entire system to attain equilibrium. The volume is adjusted to maintain constant pressure at the desired temperature. Calculation of the diffusion coefficient then proceeds by recording all changes in position of the split interstitial.

### III. DETAILED KINEMATICS OF THE DIFFUSION PROCESS

The equilibrium position of the split interstitial places the axis of the dumbbell along a  $\langle 110 \rangle$  di-

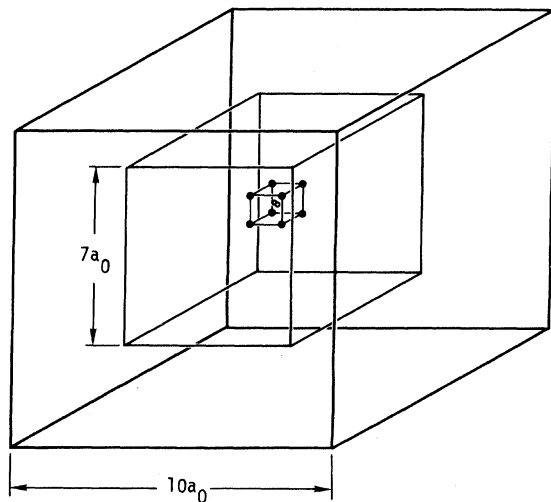


FIG. 1. Calculation grids showing relative sizes in comparison to a single central unit cell containing the split interstitial. The dynamic and selected static calculations were done in the  $(10a_0)^3$  cell, survey static calculations in the smaller  $(7a_0)^3$  cell.

rection and, as shown in Fig. 2(a), the interstitial atoms are themselves contained within a  $\{001\}$  plane with the interstitial centered about  $(0, 0, 0)$ . Note that in our nomenclature, lengths are defined in units of *half a lattice*; e.g., atom 3, the cube center in Fig. 2(a), is at  $(1, 1, 1)$ .

The execution of a diffusive jump involves a center-of-mass displacement of the dumbbell in Fig. 2(a) more or less along  $[111]$ , followed by the displacement of atom 3 parallel to  $[011]$ . The final position of the interstitial now centered about  $(1, 1, 1)$  after a single jump is shown by Fig. 2(b), in which the axis of the dumbbell is no longer along  $[110]$ , but rather parallel to  $[011]$ . If the dumbbell's center-of-mass motion had displaced atom 3 along  $[101]$  instead of  $[011]$ , the resulting final configuration would be that shown in Fig. 2(c). Again, the dumbbell is centered at  $(1, 1, 1)$ , but its axis is now parallel to  $[101]$ .

We now examine alternative jumps that the interstitial shown in Fig. 2(a) can make. Displacement along  $[1\bar{1}\bar{1}]$  would lead to a jump to the atom site in the cell directly below atom 3. These two jumps,  $[111]$  and  $[1\bar{1}\bar{1}]$ , and their inverses  $[\bar{1}\bar{1}1]$  and  $[\bar{1}1\bar{1}]$ , have equal *a priori* probability if random motion prevails, and they account for four of the eight neighboring sites into which the interstitial can jump. In order to reach any of the remaining four sites, the interstitial must first rotate. It is clear that rotation of the dumbbell axis by  $90^\circ$  around  $[001]$  [shown in Fig. 2(d)] results in an equilibrium  $[\bar{1}10]$  orientation from which all four remaining sites can be reached. The intermediate

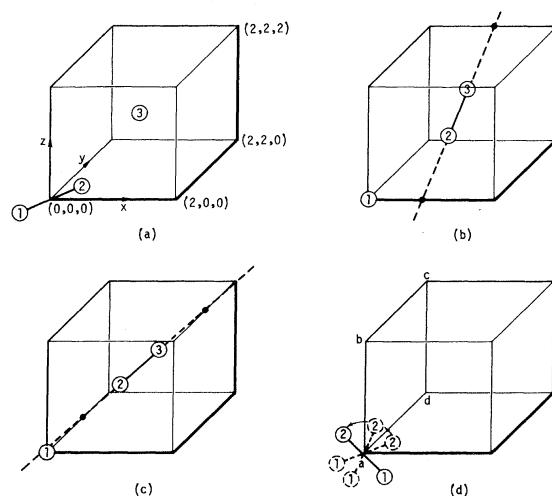


FIG. 2. (a) An interstitial dumbbell centered about  $(0, 0, 0)$  can move via a diffusive jump to positions (b) or (c) with equal *a priori* probability, or the dumbbell can rotate (d) and then diffuse as described in the text.

position contained within the (100) plane, viz.,  $(abcd)$  in Fig. 2(d), is the equilibrium  $[011]$  orientation. From this orientation, only two of the remaining four sites can be reached. Neighboring sites in a direction normal to the dumbbell axis cannot be reached by a simple diffusive jump, but require at least one rotation prior to jumping.

The split interstitial maintains a nearly constant distance of separation between its two members, irrespective of orientation. The major motion occurs as a displacement of the entire unit, so one might say that the acoustic rather than the optic mode dominates. This is true even as the prospective jumping atom approaches the saddle point. A computation run at 0.05 eV for a time long enough to observe several diffusive jumps verifies this picture. Unfortunately, this is difficult to verify in the temperature range within which diffusion coefficients actually were determined owing to the large thermal displacements of all the atoms.

#### IV. RESULTS OF DYNAMIC CALCULATION

##### A. Dynamic calculation of the diffusion coefficient

It is difficult to establish the discreteness of a diffusive jump, since large center-of-mass motions that do not necessarily give rise to diffusion occur. These motions are merely vibrational excursions about the equilibrium lattice position. TBP divided their lattice into Wigner-Seitz cells, and defined the cell that contained two atoms longer than one free period of oscillation as the equilibrium position of the interstitial. We found that this method yielded spuriously low values for the activation enthalpy of motion ( $\Delta H_m^+$ ). Consequently, we used two other mutually independent methods of calculating  $D$ , one of which relies upon the movement of the center of mass of the split interstitial and the other upon the total root-mean-square distance of travel of the defect.

The split-interstitial defect is defined as centered on a lattice site from which neither atom is within  $\frac{1}{3}$  of a lattice constant  $a_0$ . The first method records a jump when both the vacant center of mass, thus defined, and the additional interstitial atom transfer to an adjacent site; no residence time upon either location is required in order for such motion to qualify as a true diffusive displacement. The diffusion coefficient now can be calculated from the mean jump rate  $\Gamma^2$  (average number of displacements per unit time) by

$$D = \Gamma a_0^2 / 8. \quad (1)$$

In the absence of correlation effects, this value should agree with that calculated from a macroscopic continuum or random-walk definition, i.e.,

$$D = \langle R^2 \rangle / 6t_0, \quad (2)$$

where  $\langle R^2 \rangle$  is the mean-squared displacement after a lapse of time  $t_0$ . It is this latter value that is of interest, since it is independent of the choice of jump criterion as long as  $t_0 > \Gamma^{-1}$ . Because of the necessarily *ad hoc* nature of any attempt to define the diffusion of an extended defect in terms of a series of discrete displacements, we feel that the macroscopic approach is required if one wishes to make a valid comparison between dynamic and static calculations.

Calculations were made at five temperatures from 0.08 to 0.3 eV ( $0.25 < T/T_m < 0.95$ ). At each temperature, the interstitial was allowed to diffuse until 1000 or more jumps, defined by the criteria given above, were accumulated. Each run was arbitrarily divided into  $n$  segments of equal duration, and  $\langle R^2 \rangle$  was computed. The number of segments was varied from 1 to 200. In order to calculate  $D$  we take  $\langle R^2 \rangle / 6t_0$  in Eq. (2) as the average of all the values obtained. A normalized plot of the values of  $\langle R^2 \rangle / 6t_0$  obtained is shown in Fig. 3 for the data at  $T = 0.297$  eV. As the figure shows, considerable fluctuation is observed. The values of the diffusion coefficient  $D$  from Eq. (2) are shown in Fig. 4 as a function of  $T_m/T$ .

A least-squares fit of the data to Eq. (3) was used to evaluate  $\Delta H_m^+$  and  $D_0$ ,

$$D = D_0 \exp(-\Delta H_m^+ / kT), \quad (3)$$

with  $D_0 = 2.19 \times 10^{-3}$  cm<sup>2</sup>/sec and  $\Delta H_m^+ = 0.365$  eV. Arrhenius behavior thus is observed over the whole range of temperatures investigated.

##### B. Comparison of counting methods

TBP obtained Arrhenius behavior, but only over the higher-temperature portion of their work. In

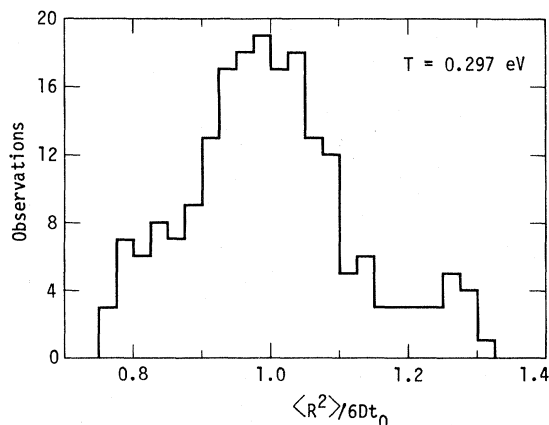


FIG. 3. Distribution of  $\langle R^2 \rangle / 6t_0$  about the average value ( $D$ ) at  $T = 0.297$  eV.



of  $\frac{1}{2}$  (corresponding to forbidden rotation) and  $\frac{1}{4}$  (corresponding to random diffusion).  $P$  (see the Appendix) can be calculated as follows from the average number of jumps  $\langle n \rangle$  between changes in  $\langle 111 \rangle$  axes:

$$\langle n \rangle = 1/(1 - P). \quad (4)$$

The results shown in Table I reveal that only at the lowest temperatures does  $P$  even begin to approach a value as low as  $\frac{1}{2}$ , while at high temperatures the probability of continuing along the same axis reaches values as high as 0.84.

An additional verification of the statistical validity of describing the results in terms of a continuing probability is afforded by the calculation of the distribution of straight-line segments (see Fig. 6), i.e., the linear paths connecting the nodes where a change of direction occurs. Using the experimental values of  $P$  listed in Table I and the analysis provided in the Appendix, the distribution of linear segments shown in Fig. 7 was back-calculated and compared to the experimentally observed distribution. It should be emphasized that experimental values of  $P$  are derived from the average number of jumps per segment length and are not calculated explicitly from the distribution of segment lengths. The results shown in Fig. 7 are for the minimum and maximum correlation effects, viz.,  $T = 0.082$  eV and  $T = 0.196$  eV, with the broken histogram representing the calculated values and the solid histogram the observed ones. The agreement is quite good, and the existence of such a nonrandom path will be shown to be the result of the interplay of the jump geometry with the shape of the static potential and temperature dependence of the kinematics.

## V. STATIC POTENTIAL

To allow comparison with the fully dynamic calculation, the static potential has been calculated by a dynamic relaxation method applied to a matrix volume consisting of a block of  $7 \times 7 \times 7$  cells corresponding to 432 atoms. This unit was selected after a comparison with a larger block of  $10 \times 10 \times 10$  unit cells containing 1458 atoms failed

to reveal a significant difference for selected test calculations. The matrix is constrained to constant volume, and the interstitial atom is held at selected positions on the surface of a Wigner-Seitz cell fixed with respect to the corner atoms of the block. The temperature of the ensemble is raised a few hundredths of an eV in the usual manner, by imparting a random velocity to each of the atoms. The ensemble will continue to fluctuate about the true minimum energy for inconveniently long periods of time unless one introduces some means of damping the vibrations. This is done by temporarily setting equal to zero the motion of all atoms whose velocity, at the chosen instant, is decreasing. The constraint is then removed, and the process is repeated until there is no further change in the total potential energy of the entire system. We have dubbed this method "dynamic relaxation," and its essential aim is to eliminate the possibility of the system falling into a local metastable equilibrium.

The energies of the split interstitial oriented along the three major crystallographic directions, viz.,  $\langle 100 \rangle$ ,  $\langle 110 \rangle$ , and  $\langle 111 \rangle$ , have been calculated by the dynamic relaxation method. Because the  $\langle 100 \rangle$  and  $\langle 111 \rangle$  are completely unstable with re-

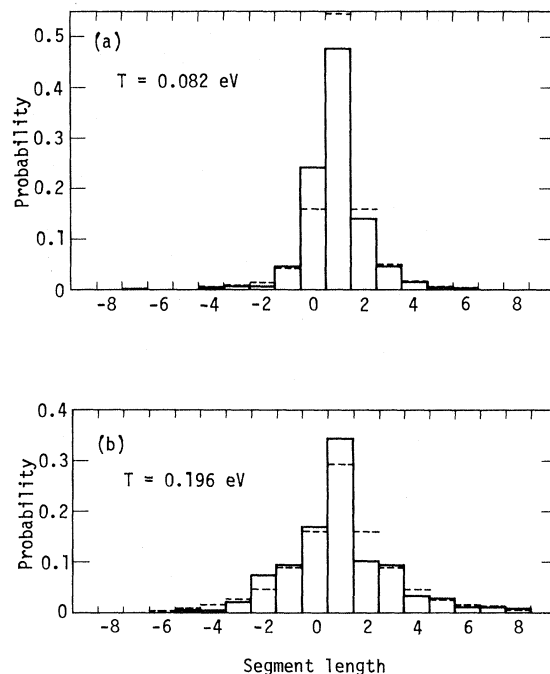


FIG. 7. Comparison of the observed segment length distribution with that calculated using the average value of the number of jumps per segment and equations given in the Appendix. The solid bars show the observed, and the dotted bars the calculated distributions.

TABLE I. Jump sequences.

$T$ (eV)	$\langle n \rangle$	$P$
0.082	2.18	0.54
0.102	2.45	0.59
0.153	5.59	0.82
0.196	6.11	0.84
0.297	4.79	0.79

spect to  $\langle 110 \rangle$ , it is necessary to restrain the dumbbell artificially in these configurations. This is done by translating one of the members of the dumbbell along either of these directions until the second member is repelled to a position equidistant from the rational lattice point, about which the interstitial is then centered. The dynamic relaxation procedure is then applied while holding the first member of the dumbbell fixed, and the energy of the configuration is computed in the normal way. The equilibrium configuration, viz., the  $\langle 110 \rangle$ , is automatically attained with no constraints. Unlike bcc iron, for which the  $\langle 111 \rangle$  contains a local minimum in the potential energy giving rise to a metastable condition,<sup>2</sup> in tungsten all positions except  $\langle 110 \rangle$  are completely unstable. However, the relative difference in energy between them is the same for iron. The results obtained for the  $10 \times 10 \times 10$  cell are listed in Table II taking the split  $\langle 110 \rangle$  as the standard state. In all three cases, the split configuration has a lower energy than that corresponding to a single interstitial atom located equidistant from two lattice sites, i.e., at the surface of the Wigner-Seitz cell. The energy of three additional configurations on the Wigner-Seitz surface (corresponding to a tetrahedral site), the saddle point for diffusion, and the minimum energy found on the  $\langle 100 \rangle$  face are also listed. Table II also lists, in the notation of Sec. II, the coordinates of the interstitial in each configuration. The energies given correspond to the change in internal energy at constant volume. However, they also correspond to the change in enthalpy at constant pressure since both represent the work done on the system in going from the equilibrium configuration to any of the other configurations. This was verified for several non-equilibrium configurations by expanding the crystal until the pressure dropped to match that in the equilibrium configuration. In particular, this procedure gave an activation volume at the saddle point of 0.1 of an atomic volume.

Figure 8 shows a Wigner-Seitz cell with the major crystallographic directions designated.

Because of symmetry, the region bounded by  $\langle 100 \rangle$ ,  $\langle 111 \rangle$ , and  $\langle 110 \rangle$  is a complete representation of the entire crystal structure. The  $\langle 100 \rangle$  and  $\langle 111 \rangle$  are normal to the respective faces, but  $\langle 110 \rangle$  intersects the Wigner-Seitz surface at the boundary between two  $\{111\}$  planes. Point  $e$  is the location of the interstitial in its equilibrium position. Plotting the energy of the dumbbell requires mapping the potential as a function of six independent coordinates. To reduce the problem to manageable proportions, we define the interstitial as the member of the dumbbell farthest from the lattice site, and we consider a subset of the configuration space of the dumbbell that considers only at the position of this outermost interstitial, allowing the inner partner to seek the position that minimizes the energy of the entire configuration. This greatly reduces the volume of the Wigner-Seitz cell that must be considered. If we move the interstitial from the surface in toward the cell center, at some point its opposite number will be moved farther from the center, and the position of the interstitial, as previously defined, will simply shift to the opposite side of the Wigner-Seitz cell. Since the separation of the pair was found to be nearly independent of orientation, the surface forming this inner boundary will be approximately a sphere centered about the origin and intersecting point  $e$ . Thus we need only consider the small volume contained between the sphere and the surface of the Wigner-Seitz cell. The  $7 \times 7 \times 7$  cell chosen for this mapping does introduce some distortion in the potential owing to the nearness of the fixed corner atoms. However, the errors are small, and for the purpose of delineating the general features, the method is sufficiently accurate. The enthalpy within this volume was calculated at approximately 100 different locations, 80 on the surface of the Wigner-Seitz cell and 20 within the volume. For all orientations, the energy is lower within the Wigner-Seitz cell than for one atom located on the surface. Since the interstitial must pass through the cell surface in order to execute a diffusive jump, all saddle points must lie some-

TABLE II. Interstitial energy differences.

Orientation	Split interstitial		Mono-interstitial	
	$\Delta E$ (eV)	Position	$\Delta E$ (eV)	Position
$\langle 110 \rangle$	0.00	(0.53, 0.53, 0.00)	0.64	(0.75, 0.75, 0.00)
$\langle 111 \rangle$	0.94	(0.44, 0.44, 0.44)	0.95	(0.50, 0.50, 0.50)
$\langle 100 \rangle$	1.98	(0.75, 0.00, 0.00)	2.08	(1.00, 0.00, 0.00)
Tetrahedral	...	...	1.38	(1.00, 0.50, 0.00)
Saddle point	...	...	0.38	(0.65, 0.65, 0.20)
Minimum (100 face)	...	...	0.64	(1.00, 0.25, 0.25)

where on the Wigner-Seitz surface. The contours generated by connecting equal values of the energy are shown in the exploded views of the  $\{100\}$  and  $\{111\}$  surfaces presented in Fig. 9. There are six equivalent minima that lie on  $\{111\}$ . They are labeled S. That the six minima are not entirely equivalent is shown in Fig. 9; nevertheless, the  $\langle 111 \rangle$  face must exhibit mirror symmetry across the corners of the hexagon. This is required because an interstitial leaving the Wigner-Seitz cell on one side of this mirror plane enters the next cell in the reflected position on the opposite side. The minima must therefore be equal. The distortion in the present case is due to the smaller size of our computational block, as previously mentioned. In the  $10 \times 10 \times 10$  crystal, the values of the energy at both minima were identical to within a few thousandths of an eV. In his calculations for  $\alpha$ -Fe, Johnson<sup>4</sup> found that the minima were at the position marked X in Fig. 9. This is a configuration also having sixfold symmetry, and an atom exiting such positions enters the next Wigner-Seitz cell in an equivalent position. The topographic features of the surface are probably better illustrated in the three-dimensional view shown in Fig. 10. Here, the surface of the Wigner-Seitz cell is plotted on a standard stereographic triangle. Again, the two minima are labeled S. From this graph, it is apparent that the saddle point is more properly termed a saddle trough, since the ridge separating the two minima is only 0.03 eV high. In Fig. 11, a three-dimensional view of the energy

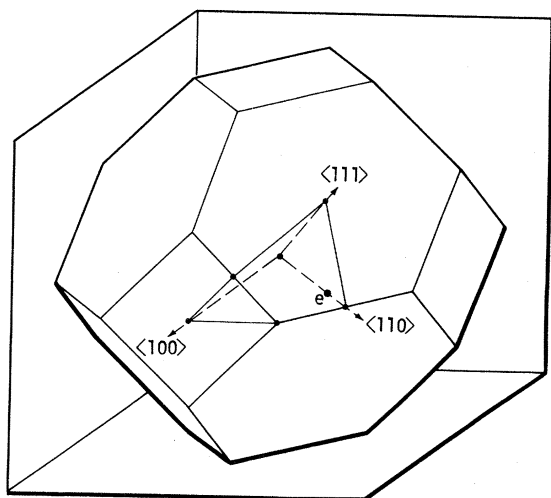


FIG. 8. Wigner-Seitz cell for the bcc lattice. Static calculations of the energy were made for 80 points on the surface and 20 within the volume of the cell. The area bounded by lines between  $\langle 100 \rangle$ ,  $\langle 110 \rangle$ , and  $\langle 111 \rangle$  uniquely represents the entire surface.

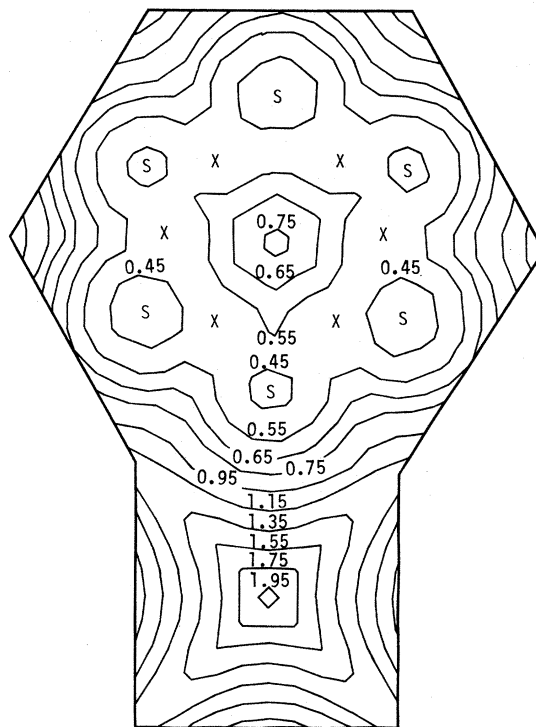


FIG. 9. Orthographic projection of the two surfaces of the Wigner-Seitz cell showing contours of equal energies of activation in eV, computed by arbitrarily fixing the coordinates of one member of the split interstitial on the surface shown in Fig. 8 and allowing all other atoms to move freely, seeking the minimal energy of the entire ensemble.

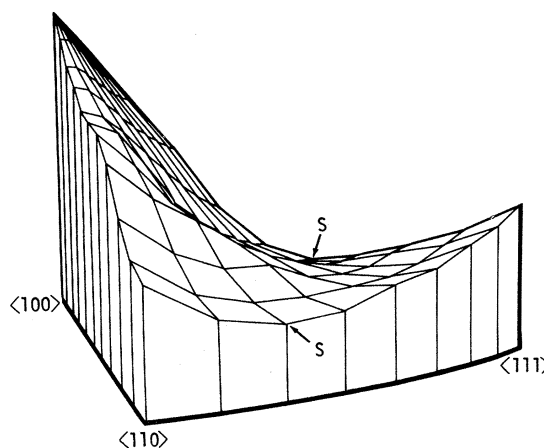


FIG. 10. Stereographic projection of the energy surface shown in Fig. 9.

on the interior surface of the Wigner-Seitz cell, i.e., the sphere corresponding to the equilibrium radius, is plotted. Here the deep minima at the equilibrium configuration  $\langle 110 \rangle$  is clearly seen. The potential rise is very rapid, attaining values very near to those on the surface of the Wigner-Seitz cell in all other orientations. Since the energy increases monotonically outward from this surface to the surface of the cell, any path on this surface represents a minimum energy path for all changes of orientation of the interstitial. Point *R* in the center of the stereo triangle thus corresponds to the barrier opposing rotation, and it is located at the position of the saddle point in Fe found by Johnson. Correspondingly, Johnson found that the barrier for a rotation corresponded to our saddle point. To complete the rotation, the interstitial would have to cross the line connecting  $\{100\}$  and  $\{111\}$ , then proceed back over another equivalent ridge to an alternate  $\{110\}$  orientation; the rotation barrier is double-humped in this case. The dimple corresponds approximately to 0.03 eV, while the rotation barrier corresponds to 0.37 eV.

## VI. DISCUSSION

### A. Activation enthalpy

A comparison of static and dynamic results should begin with a comparison of the activation enthalpies obtained by both methods. In the present case, the dynamically determined enthalpy of 0.365 eV is approximately 5% lower than that determined statically, viz., 0.38 eV. This difference would appear to be well within the uncertainty in both methods.

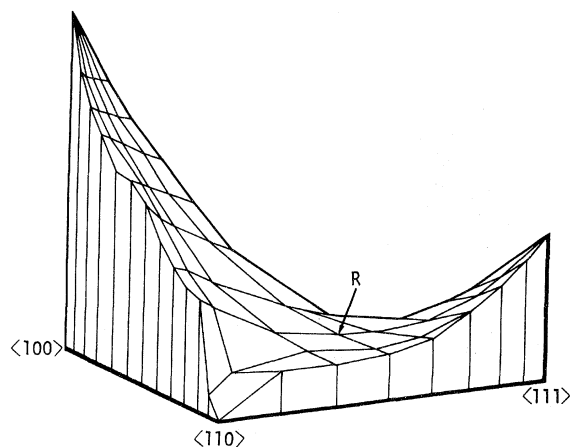


FIG. 11. Stereographic projection of the energy surface generated by allowing the dumbbell axis to assume orientations in all representative directions while maintaining each member of the interstitial dumbbell equidistant from the center.

In addition to normal  $\langle 111 \rangle$  diffusive jumps, it is possible for the interstitial to jump directly to a second-neighbor site. Such jumps correspond to leaving the Wigner-Seitz cell through the  $\{100\}$  face (Fig. 8). From the static calculations (Table II), the minimum energy required is 0.64 eV. Dynamically, such jumps were observed at the four highest temperatures, a few at 0.1 eV and about 20 at 0.297 eV. This ratio is again consistent with the static enthalpy.

### B. Kinematics

The influence of the static potential on the details of the diffusion kinematics is clearly revealed in Figs. 12 and 13. In Fig. 12(a), the positions of an interstitial just before a successful jump to the next site are plotted on the standard stereographic triangle. As shown, the exit points of the interstitial are clustered at the saddle point

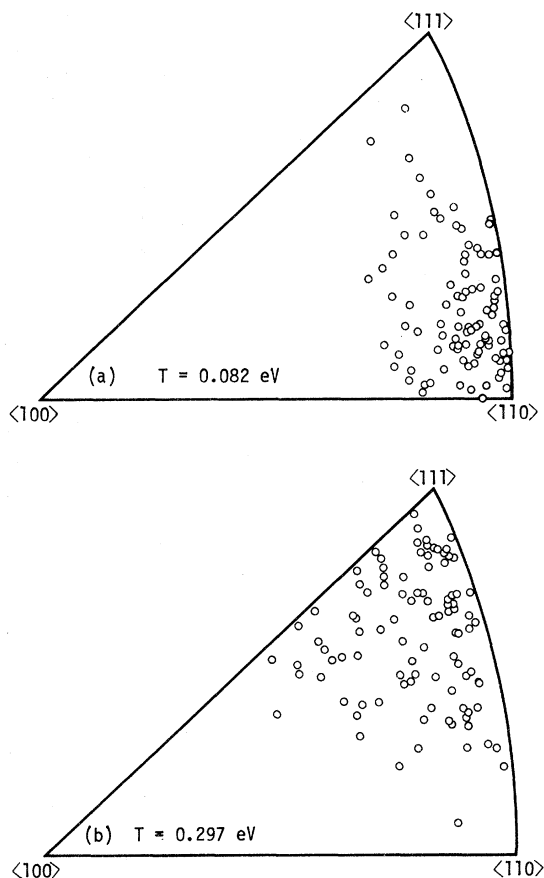


FIG. 12. Stereo map showing points at which the interstitial atoms changed Wigner-Seitz cells. Note that in (b) the relative density is shifted upward toward the  $\langle 111 \rangle$  at the higher temperature relative to (a), which is shifted toward  $\langle 110 \rangle$ . This is consistent with the static potential calculations.



nearest the equilibrium site. The further saddle point, which, as expected, requires some reorientation of the interstitial, is only sparsely populated. Note that this figure is for  $T = 0.08$  eV, a relatively low temperature. Figure 12(b) is a similar diagram for  $T = 0.297$  eV, and at this higher temperature, the points are distributed much more uniformly, although they are obviously still confined to the trough region shown in the three-dimensional potential plot. Figure 13(a), a typical path of an interstitial between jumps, is shown on a stereo triangle, and the plot is again for the lower temperature, viz.,  $T = 0.08$  eV. The interstitial enters near the upper saddle point, indicating that it left the previous cell at the lower saddle point, which is connected to the equilibrium configuration by a center-of-mass displacement. The interstitial now reorients, and in a few vibrational periods, it reaches and remains near the equilibrium configuration until a fluctuation eventually causes it to diffuse out through the lower saddle point. Figure 13(b) is a similar graph for  $T = 0.297$  eV. At this higher temperature, the interstitial diffuses for a much shorter time before jumping, and the displacement initiated is actually from a position in the *middle* of the connecting trough, but not close to either saddle point. Since the interstitial always enters a new cell in an excited state, i.e., in an orientation other than one near equilibrium, it takes a finite time for the dumbbell and its neighboring atoms to reorient. Typically, two to three lattice periods are required. This time was estimated by looking at a dozen or so typical jump sequences like those illustrated in Fig. 13. At low temperatures, the average time between jumps is 20 lattice-vibration periods, whereas at high temperatures, the average between jumps is approximately  $1\frac{1}{2}$  lattice-vibration periods. At high temperatures, therefore, the equilibrium position is generally not attained before the next jump occurs. Thus, the topographic features of the static potential are revealed by the jump process as well as by the interstitial movement between jumps.

### C. High-temperature correlation

In the bcc lattice, it is possible for the  $\langle 110 \rangle$ -split interstitial to diffuse back and forth along a given  $\langle 111 \rangle$  axis without returning to the equilibrium configuration. A change of axis requires that the dumbbell rotate through a configuration near equilibrium, since the energy at other points on the  $\{010\}$  plane required for an axis change have energies much too high. At high temperatures, the interstitial executes a diffusive dump in times comparable, on the average, to that required for reorientation into a near-equilibrium

configuration. Furthermore, because of the pre-exponential entropy term, viz., the larger number of available states, the probability of arriving and continuing to exist after a jump in an excited state is high. Thus, between jumps, the dumbbell seldom attains the equilibrium position, and diffusion tends to proceed along the same direction. At low temperature, the activation-energy term dominates, and the mean time between diffusion jumps is much longer than the time required to reorient to a near-equilibrium configuration. The dumbbell spends most of its time near the equilibrium position, and consequently, it changes direction more often between diffusion jumps. This accounts for the high degree of directional correlation as well as the increase of directional correlation with temperature.

### VII. CONCLUSIONS

The activation enthalpy of 0.365 eV determined dynamically is within 5% of the value (0.38 eV)

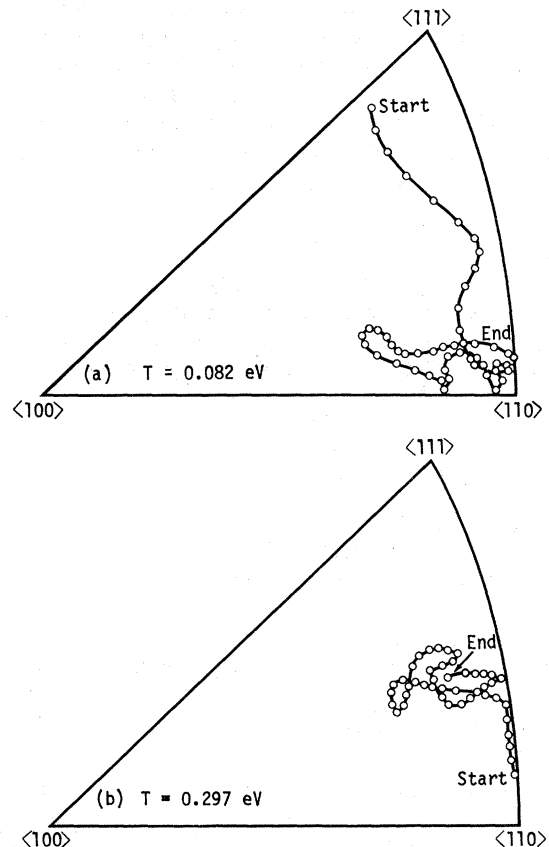


FIG. 13. (a) Typical path of an interstitial atom between jumps for a relatively low temperature. Note how the atom enters the cell at a position corresponding to the upper saddle point and exits through the lower one. (b) At a higher temperature the atom exits near the middle of the trough.

determined by the static relaxation method. This is well within the uncertainties in the two methods, and we conclude, in view of both the present results and those of TBP, that static methods can accurately predict the enthalpy of diffusion of interstitial defects, within the usual limitations imposed by computer simulation. Furthermore, many of the general features of the diffusion process can be inferred from the structure of the static potential.

Dynamic calculations must be extended to times long enough to define macroscopic random-walk diffusion coefficients, since no completely satisfactory method has been found to describe the interstitial motion as a series of discrete jumps. This may be due in part to the extended nature of the defect and to the fact that the reference coordinate system against which motion is measured is based upon the undistorted perfect lattice.

The observed high-temperature correlation should prove to be a general feature of split  $\langle 110 \rangle$  interstitial diffusion in the bcc lattice, arising as it does from a combination of geometry and entropy effects. Macroscopically, the effect is of little consequence. Locally, on a 100-Å scale, the one-dimensional nature of the diffusion could substantially modify expected recombination and recovery kinetics of radiation damage.

#### ACKNOWLEDGMENTS

The authors express appreciation to Dr. W. D. Wilson for his occasional assistance and enlightening discussions. They also wish to thank J. Kinney, T. Riffle, and P. Fronberg for their timely computational help.

#### APPENDIX: INTERSTITIAL DIFFUSION

Suppose an interstitial atom changes its direction of travel and takes  $n$  jumps along a new line. If  $P$  is the probability that any new jump continues along this line, the probability of having a total of  $n$  jumps along the line is  $(1-P)P^{n-1}$ .  $\langle n \rangle$ , the average number of jumps along a line, is given by

$$\langle n \rangle = (1-P) \sum_{n=0}^{\infty} n P^{n-1} = \frac{1}{1-P}.$$

Let  $P_n(r)$  be the probability that an atom will make  $n$  jumps along a line, return to  $r$  units of its starting position, and then jump in a different direction. We assume that forward and backward jumps are equally likely and are uncorrelated. Again, the probability of changing direction is  $P$ .

Let  $N_+$  be the number of jumps in the same direction as the first jump. Let  $N_-$  be the number of jumps in the opposite direction.

#### 1. Special case of $r = 0$

$$N_+ = N_-$$

and

$$N_+ + N_- = n.$$

Since the jump series is terminated after the  $n$ th jump, the probability  $P_n(0)$  is proportional to  $1-P$ . Also, each jump after the first jump (which occurs with probability 1) has a probability of  $P/2$ . ( $P$  to stay on the line and  $\frac{1}{2}$  to move in either the  $+$  or  $-$  direction.) Thus,

$$P_n(0) = (1-P) \left(\frac{P}{2}\right)^{n-1} \frac{(n-1)!}{(N_+-1)!(N_-)!} \quad (n \text{ even}).$$

The last term represents the number of possible configurations in which the  $n-1$  jumps (the first jump is certain) can occur.

In this case,

$$N_+ = N_- = n/2$$

and

$$P_n(0) = (1-P) \left(\frac{P}{2}\right)^{n-1} \frac{(n-1)!}{(n/2-1)!(n/2)!}.$$

Next, sum over  $n$ :

$$P(0) = \sum_{\substack{n \geq 2 \\ n \text{ even}}} P_n(0).$$

Set

$$n = 2k+2, \quad k = 0, 1, 2, \dots$$

Then

$$P(0) = (1-P) \sum_{k=0}^{\infty} \left(\frac{P}{2}\right)^{2k+1} \frac{(2k+1)!}{k!(k+1)!}.$$

#### 2. $r > 0$

The atom can return to distance  $r$  from its starting point on either side of its original starting point. Thus there are two possibilities:

$$N_+ = N_- + r, \quad N_+ + N_- = n$$

or

$$N_- = N_+ + r, \quad N_+ + N_- = n,$$

with the solutions

$$N_+^1 = (n-r)/2, \quad N_+^2 = (n+r)/2$$

and

$$N_-^1 = (n+r)/2, \quad N_-^2 = (n-r)/2.$$

Then

$$P_n(r) = (1-P) \left(\frac{P}{2}\right)^{n-1} (n-1)! \times \left[ \frac{1}{(N_+^1-1)!(N_-^1)!} + \frac{1}{(N_+^2-1)!(N_-^2)!} \right],$$

with  $n$  and  $r$  both even or both odd, and with  $n \geq r$ .

$$\begin{aligned}
P_n(r) &= (1-P) \left(\frac{P}{2}\right)^{n-1} (n-1)! \left[ \frac{1}{[(n+r-2)/2]! [(n-r)/2]!} + \frac{1}{[(n-r-2)/2]! [(n+r)/2]!} \right] \\
&= (1-P) \left(\frac{P}{2}\right)^{n-1} (n-1)! \left[ \frac{(n+r)/2 + (n-r)/2}{[(n+r)/2]! [(n-r)/2]!} \right] = (1-P) \left(\frac{P}{2}\right)^{n-1} \frac{n!}{[(n+r)/2]! [(n-r)/2]!}, \\
P(r) &= (1-P) \sum_{\substack{n, r \\ \text{both even} \\ \text{or both odd}}} \left(\frac{P}{2}\right)^{n-1} \frac{n!}{[(n+r)/2]! [(n-r)/2]!}.
\end{aligned}$$

Set  $n = 2k + r$ ,  $k = 0, 1, 2, \dots$ :

$$P(r) = (1-P) \sum_{k=0}^{\infty} \left(\frac{P}{2}\right)^{2k+r-1} \frac{(2k+r)!}{(k+r)! k!}.$$

Note that

$$P(1) = (1-P) \sum_{k=0}^{\infty} \left(\frac{P}{2}\right)^{2k} \frac{(2k+1)!}{(k+1)! k!}$$

and

$$P(0) = (P/2) P(1). \quad (\text{A1})$$

We will now evaluate  $P(0)$ ,  $P(1)$ , and  $P(2)$ :

$$\begin{aligned}
P(0) &= (1-P) \sum_{k=0}^{\infty} \left(\frac{P}{2}\right)^{2k+1} \frac{(2k+1)!}{k! (k+1)!} \\
&= \frac{(1-P)}{P} \sum_{n=1}^{\infty} \left(\frac{P}{2}\right)^{2n} \frac{(2n)!}{n! n!},
\end{aligned}$$

but

$$\frac{1}{(1-P^2)^{1/2}} = \sum_{n=0}^{\infty} \left(\frac{P}{2}\right)^{2n} \frac{(2n)!}{n! n!};$$

therefore,

$$P(0) = \frac{1-P}{P} \left[ \frac{1}{(1-P^2)^{1/2}} - 1 \right], \quad (\text{A2})$$

therefore,

$$P(1) = \frac{2(1-P)}{P^2} \left[ \frac{1}{(1-P^2)^{1/2}} - 1 \right] \quad [\text{from (A1)}].$$

(A3)

$$P(2) = (1-P) \sum_{k=0}^{\infty} \left(\frac{P}{2}\right)^{2k+1} \frac{(2k+2)!}{(k+2)! k!}$$

$$\begin{aligned}
P(r+1) - \frac{P}{2} P(r) &= (1-P) \sum_{k=0}^{\infty} \left[ \left(\frac{P}{2}\right)^{2k+r} \frac{(2k+r+1)!}{(k+r+1)! k!} - \left(\frac{P}{2}\right)^{2k+r} \frac{(2k+r)!}{(k+r)! k!} \right] \\
&= (1-P) \sum_{k=0}^{\infty} \left(\frac{P}{2}\right)^{2k+r} \frac{(2k+r)!}{(k+r)! k!} \left[ \frac{2k+r+1}{k+r+1} - 1 \right] \\
&= (1-P) \frac{P}{2} \sum_{k=0}^{\infty} \left(\frac{P}{2}\right)^{2k+r+1} \frac{(2k+r+2)!}{(k+r+2)! k!} = (P/2) P(r+2);
\end{aligned}$$

Therefore for  $r > 0$ ,

$$P(r+2) = (2/P) P(r+1) - P(r). \quad (\text{A5})$$

To evaluate, start with

$$\sum_{k=0}^{\infty} \left(\frac{P}{2}\right)^{2k+1} \frac{(2k+1)!}{k! (k+1)!} = \frac{1}{P} \left[ \frac{1}{(1-P^2)^{1/2}} - 1 \right].$$

Multiply by  $P/2$ , and take the derivative with respect to  $P$ . Then,

$$\sum_{k=0}^{\infty} \left(\frac{P}{2}\right)^{2k+1} \frac{(2k+2)!}{k! (k+1)!} = \frac{P}{(1-P^2)^{3/2}}.$$

Multiply through by  $P/2$ , and integrate with respect to  $P^2/2$ :

$$\begin{aligned}
\int d \left(\frac{P}{2}\right)^2 \sum_{k=0}^{\infty} \left(\frac{P}{2}\right)^{2k+2} \frac{(2k+2)!}{k! (k+1)!} \\
= \int_0^P d \left(\frac{P}{2}\right)^2 \frac{P^2}{2} \frac{1}{(1-P^2)^{3/2}}
\end{aligned}$$

or

$$\begin{aligned}
\left(\frac{P}{2}\right)^3 \sum_{k=0}^{\infty} \left(\frac{P}{2}\right)^{2k+1} \frac{(2k+2)!}{k! (k+2)!} \\
= \frac{1}{4} \left[ (1-P^2)^{1/2} + \frac{1}{(1-P^2)^{1/2}} - 2 \right]
\end{aligned}$$

or

$$P(2) = \frac{2(1-P)}{P^3} \left[ (1-P^2)^{1/2} + \frac{1}{(1-P^2)^{1/2}} - 2 \right]. \quad (\text{A4})$$

$P(r)$  for larger values of  $r$  can be determined by using the recursion relation developed as follows:

\*This work was performed under the auspices of the U.S. Energy Research and Development Administration, under contract No. W-7405-Eng-48.

<sup>1</sup>D. H. Tsai, R. Bullough, and R. C. Perrin, J. Phys. C 3, 2022 (1970).

<sup>2</sup>R. A. Johnson and W. D. Wilson, in *Proceedings of the International Conference on Interatomic Potentials and*

*Simulation of Lattice Defects*, edited by P. C. Gehlen, J. R. Beeler, Jr., and R. I. Jaffee (Plenum, New York, 1972), p. 301.

<sup>3</sup>B. J. Alder, D. M. Gass, and T. E. Wainwright, J. Chem. Phys. 53, 3813 (1970).

<sup>4</sup>R. A. Johnson, Phys. Rev. 134, A1329 (1964).